Research Article Vol. 33, No. 20 / 6 Oct 2025 / Optics Express 42408
Optics EXPRESS

High-speed integrated silicon germanium optical modulator with 3 GHz bandwidth in the 5-9 µm wavelength range

JAVIER HUERTAS-PEDROCHE,[1,*] VICTOR TURPAUD,[1] LUCA LUCIA,[1] ADEL BOUSSEKSOU,[1] THI HAO NHI NGUYEN,[1] HAMZA DELY,[1] GIA LONG NGO,[1] STEFANO CALCATERRA,[2] DAVIDE IMPELLUSO,[2] AFONSO DE CERDEIRA OLIVEIRA,[2] ETIENNE HERTH,[1] DAVID BOUVILLE,[1] SAMSON EDMOND,[1] JEAN RENE COUDEVYLLE,[1] VICTOR MERUPO,[3] EMILIEN PEYTAVIT,[3] JEAN-FRANÇOIS LAMPIN,[3] STEFANO BARBIERI,[3] JACOPO FRIGERIO,[2] RAFFAELE COLOMBELLI,[1] GIOVANNI ISELLA,[2] AND DELPHINE MARRIS-MORINI[1]

[1] *Centre de Nanosciences et de Nanotechnologies, Université Paris-Saclay, CNRS, 91120 Palaiseau, France*
[2] *Dipartimento di Fisica, Politecnico di Milano, Piazza L. da Vinci, 32, 20133, Milano, Italy*
[3] *Institute of Electronics, Microelectronics and Nanotechnology, CNRS, Univ. Lille, Univ. Polytechnique Hauts-de-France, UMR 8520, F-59000 Lille, France*
[*] *javier.huertas-pedroche@universite-paris-saclay.fr*

Abstract: Mid-infrared spectroscopy is a powerful technique for identifying chemical and biological substances, increasing the demand for compact and cost-effective integrated systems. In this context, integrated electro-optic modulators are essential to implement advanced techniques such as synchronous detection or dual-comb spectroscopy. In this paper, we present a waveguide-integrated electro-optic modulator operating in a broad spectral range from 5 to 9 µm wavelength, based on a Schottky diode embedded in a graded silicon germanium waveguide. By using the free-carrier plasma absorption effect, the device achieves an extinction ratio of up to 1.9 dB at a wavelength of 9 µm. Two different methods have been used to evaluate the device speed. In both cases, high-speed operation up to 7 GHz is obtained, while the optical bandwidth is estimated to be around 3 GHz. These results represent a significant step forward in both the development of characterization techniques and in the performance of mid-IR integrated modulators, paving the way for high-performance on-chip spectroscopic systems.

1. Introduction

Mid-infrared (mid-IR) spectroscopy is a precise technique for identifying chemical and biological substances due to the presence of strong vibrational and rotational absorption bands that correspond to fundamental molecular resonances. This makes this technique extremely useful in many fields such as environmental monitoring, food safety, materials analysis or medical diagnosis [1–5]. Mid-IR spectroscopy has traditionally been limited by the dependence on bulky and expensive benchtop systems based on free-space optics. While these systems offer high performance, they are not suitable for field deployment. However, the recent development of mid-IR photonic circuits has opened up new opportunities to miniaturize spectroscopic systems, resulting in lower costs and reduced power consumption [6]. While silicon (Si) exhibits strong absorption beyond 8 µm, limiting its use at long mid-IR wavelengths [7–9], broad transparency windows in the mid-IR can be obtained using III-V materials [10], chalcogenide glasses [11],

#572563 https://doi.org/10.1364/OE.572563
Journal © 2025 Received 3 Jul 2025; revised 27 Aug 2025; accepted 14 Sep 2025; published 26 Sep 2025

Optics EXPRESS

or germanium (Ge) and silicon-germanium (SiGe) [12–18]. Interestingly, Ge and SiGe alloys combine the benefits of silicon process compatibility with the wide transparency window of Ge (up to 15 µm wavelength). Integrated photonic components, such as electro-optic modulators (EOMs), play an important role as they allow dynamic control of the optical signal, enabling amplitude or phase modulation and sensitivity enhancement via synchronous detection [19,20]. Additionally, the mid-IR range (from 2 to 20 µm wavelength) encompasses two atmospheric transparency windows (from 3 to 5 µm and from 8 to 14 µm), which are crucial for applications such as free-space communication [21,22]. This makes the development of high-speed EOMs especially important in these areas. While EOMs have achieved notable success in the near-infrared (near-IR) range, developing high-performance modulators for the mid-IR is still at its infancy. However, it can be noted that by using a InGaAs/AlInAs semiconductor heterostructure, modulation up to 20 GHz was demonstrated at 9.6 µm wavelength in a free-space amplitude modulator [23]. As an alternative approach and to obtain broadband modulation it is possible to use free carrier plasma dispersion (FCPD) or free-carriers absorption (FCA) effects which have been successfully implemented in the near-IR and short-wave mid-IR region [24,25]. Recently, FCA has been extended in the long-wave part of the mid-IR region, where a broadband integrated electro-absorption modulator has been demonstrated relying on a Schottky diode embedded in a SiGe waveguide [26]. The device modulates light over a broad wavelength range (5 to 9 µm), with demonstrated operation up to 1 GHz. However, this measurement was limited by the speed of the commercially available detector used in the experiment.

In this work, high-speed characterization of the Schottky based mid-IR integrated modulators is tackled, with the use of two different methods based on (i) the measurement of the modulated signal using a high-speed quantum well infrared photodetector (QWIP), and (ii) the development of a heterodyne technique, in which a beatnote, obtained by the combination of two modulator sidebands is measured at a low RF frequency. In both cases, high-speed operation up to 7 GHz is demonstrated, showing a significant improvement over previously reported integrated modulators in the same wavelength range.

2. Modulator design

The modulator is based on a waveguide fabricated in a 6-µm-thick graded SiGe layer, in which the material concentration increases linearly from pure Si at the bottom to pure Ge at the top. The graded layer is epitaxially grown on a 500-µm-thick heavily n-type doped Si substrate with a doping concentration of $2 \times 10^{19}\,\mathrm{cm}^{-3}$, while the graded SiGe layer exhibits a residual n-type doping concentration estimated to be in the order of 10^{15}-$10^{16}\,\mathrm{cm}^{-3}$. This linear increase in Ge concentration results in a linear increase in refractive index, from that of Si (≈ 3.4) to that of Ge (≈ 4), as illustrated in Fig. 1. The waveguide geometry is defined by etching the SiGe layer with a width and etching depth of 6 µm. This waveguide geometry provides good mode confinement at the top of the waveguide, where the refractive index is higher. Modulation via the FCPD and FCA effects is enabled via the use of a vertical Schottky diode in the waveguide core [26]. To achieve this, a metal layer is deposited on top of the waveguide core, creating a Schottky contact, while an ohmic contact is formed on the backside of the heavily doped Si substrate. High speed operation is thus ensured by the proper design of grounded coplanar waveguide (CPWG) electrodes, as shown in Fig. 1.

Simulations of the optical mode profiles are shown in Fig. 2(a) at different wavelengths (5.5, 6.4, 7.8, and 8.5 µm), considering transverse electric (TE) polarization, while electrical simulations of free carrier concentrations as a function of the voltage applied to the top contact are reported in Fig. 2(b). The simulations focus on the waveguide core, where light propagates and modulation occurs. First it can be seen that the optical modes are strongly confined near the top of the waveguide. This confinement arises from the gradual increase in the refractive index within the waveguide structure, which leads to a significant overlap between the optical modes and the

Optics EXPRESS

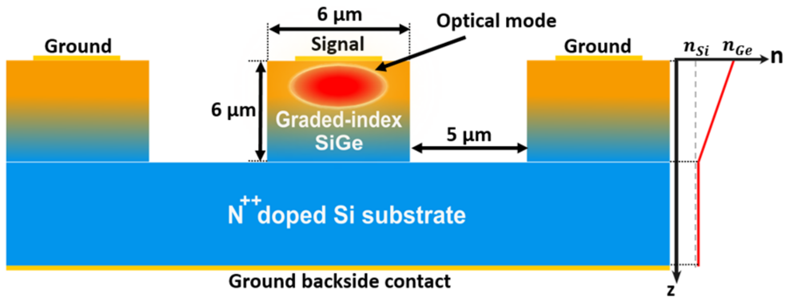

Fig. 1. Schematic cross-section of the integrated modulator showing mode confinement in the waveguide core as well as the CPWG electrode. Right: illustration of the linear variation of the refractive index as a function of the z-position.

depletion region located beneath the top Schottky contact. The depleted region can be seen in Fig. 2(b) as the dark blue area, where the electron density is below 10^{14} cm^{-3}. Interestingly, by increasing the reverse voltage applied to the top signal electrode, the depletion region is enlarged, inducing free-carrier concentration variations within the waveguide. These carrier variations modify both the refractive index and the absorption coefficient of the material. However, at long wavelengths such as those considered here, it can be shown that the refractive index variation is negligible in comparison with the absorption variation, and thus only electro-absorption modulation of the optical signal propagating in the waveguide is considered in the following.

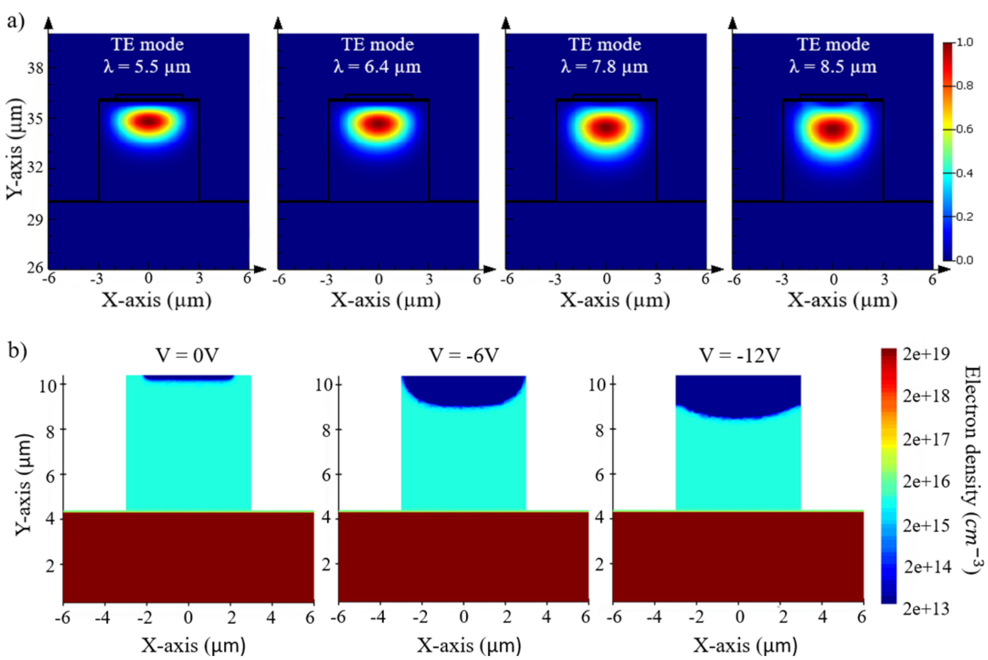

Fig. 2. a) Simulated optical mode profiles of the fundamental TE mode at different wavelengths (5.5, 6.4, 7.8 and 8.5 µm). Scale bar: normalized electric field intensity. b) Simulated electron density of the EOM at different voltages (0, −6 and −12 V), considering an n^{+}-type Si substrate with a doping concentration of 2x10^{19}cm^{-3}, and a residual doping concentration for the graded SiGe layer of 5x10^{15}cm^{-3}.

Optics EXPRESS

To achieve high speed operation, CPWG electrodes with a ground-signal-ground (GSG) configuration were used [26]. They have been designed to simultaneously achieve (i) impedance matching with the characterization equipment (50 Ohms) to obtain minimum reflection of the RF signal and optimal power transfer between the modulator and the external circuitry, (ii) speed matching between the electrical and optical signals propagating through the modulator to avoid reducing its performance, (iii) low RF losses along the CPWG electrodes. The equivalent circuit of the Schottky diode which is an RC low pass filter has been included in the CPWG electrode numerical simulations, as will be shown in the discussion section.

The complete schematic of the SiGe-integrated EOM platform based on a Schottky diode is presented in Fig. 3. At both the input and output facets, the waveguide width is set to 15 µm to facilitate efficient edge coupling with the optical beam. An adiabatic taper of 200 µm in length is then used to gradually reduce the waveguide width to 6 µm, minimizing mode mismatch and insertion loss. To interface the optical waveguide with the CPWG electrodes, additional tapers are used to expand the waveguide width to 50 µm, matching the dimensions required to contact the CPWG electrodes with external RF electrical probes. The modulator length is 1.55 mm, which appears as a compromise to achieve good modulation efficiency without increasing the loss of the device too much, as will be shown in the experimental results.

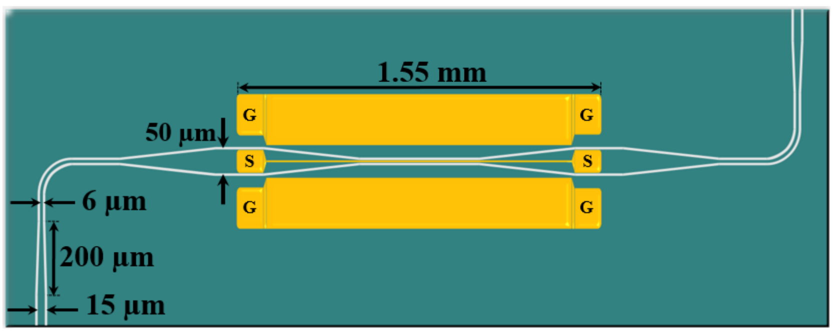

Fig. 3. Top-view schematic (not to scale) of the integrated EOM platform, illustrating both the optical waveguide and the electrical contact pads. Legend: G = Ground electrode; S = Signal electrode.

3. Fabrication

The fabrication process begins with the epitaxial growth of a 6-µm-thick graded SiGe layer, with a residual n-doped concentration estimated to be in the range of 10^{15}-10^{16} cm^{-3}, on top of a highly n-doped Si substrate (with doping concentration of 2x10^{19}cm^{-3}) by using low-energy plasma-enhanced chemical vapor deposition (LEPECVD) at a growth rate of 5-10 nm/s [27], a plasma-based variant of standard chemical vapor deposition (CVD) where the decomposition of the precursors is induced by a low energy high density argon plasma rather than thermally activated [28]. The growth rate is nearly independent of substrate temperature and is instead controlled by plasma energy and density, while the composition of the deposited layer is only determined by the precursors gas mixture introduce into the chamber. The growth process employs an argon (Ar) plasma and four different precursor molecules: germane (GeH_4), diborane ($B2H_6$), phosphine (PH_3) and silane (SiH_4). GeH_4 and SiH_4 provide Ge and Si atoms, respectively, necessary for forming the SiGe, while B_2H_6 and PH_3 act as doping agents, introducing boron or phosphorus into the SiGe layer.

For the modulator fabrication, the first lithography step defines the pattern of the top electrical contacts, followed by a deposition of 10 nm of titanium (Ti) and 300 nm of gold (Au) using electron-beam evaporation. A lift-off process is then used to remove excess metal. The optical waveguides are patterned in a second lithography step using a positive photoresist. The pattern is transferred into the SiGe layer using inductively coupled plasma reactive ion etching (ICP-RIE), achieving a 6-µm-deep etch with a vertical profile. Finally, to form the bottom electrical contact, the backside of the wafer is polished and cleaned before depositing the same Ti/Au metal stack (10-nm of Ti and 300-nm of Au) used for the top contacts. A schematic representation of the fabrication sequence is provided in Fig. 4.

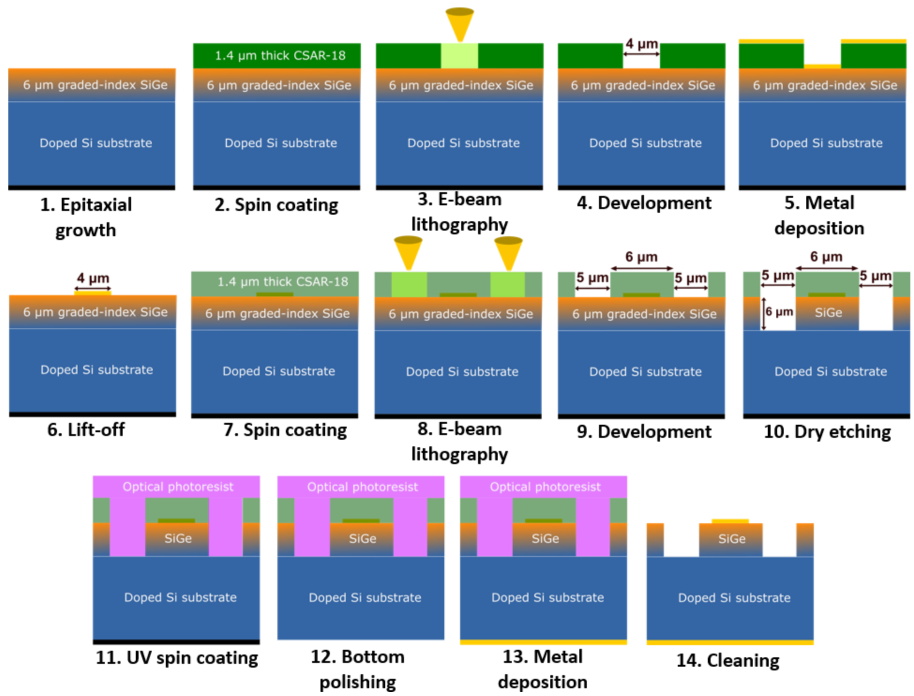

Fig. 4. Fabrication process for the electro-optical modulator based on a Schottky diode embedded in a graded-index SiGe waveguide.

4. Characterization

First, Fig. 5(a) shows the I-V characteristics of the modulator, exhibiting a rectifying behavior consistent with Schottky junction operation. This confirms the presence of a depletion region at the top of the waveguide. Analysis of the forward bias regime allows for the determination of the series resistance, which is found to be around 15 Ω. Additionally, no breakdown was observed under reverse bias up to the tested voltage range, i.e., −12 V, demonstrating good junction stability.

To evaluate the static (DC) modulation efficiency of the modulator, light from a mid-infrared quantum cascade laser (MIRcat-1400, Daylight solutions) was coupled into the waveguide. The laser was operated at a pulse repetition rate of 100 kHz with a 5% duty cycle and covered a broad spectral range from 5.5 µm to 11 µm. A DC voltage was applied to the modulator using a Keithley 2400 source-meter via GSG probes applied on the top contacts while the bottom contact is also grounded. The modulation efficiency was studied in the depletion regime. In this regime, increasing the reverse bias voltage expands the depletion region, which in turn reduces the overlap between the optical mode and the region with free carriers responsible for the absorption. This leads to a decrease in the absorption coefficient of the guided optical mode. For the DC measurement, the transmitted optical signal was detected using an external mercury

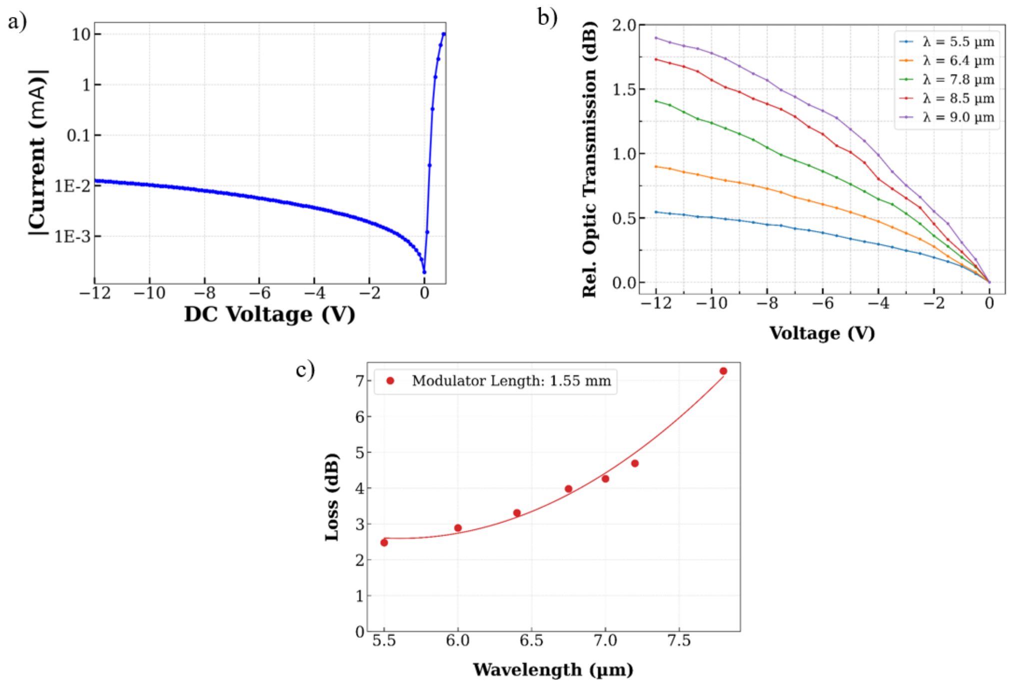

Fig. 5. a) Measured current-voltage (I-V) characteristics of the Schottky modulator. b) Relative optical transmission in the depletion regime as a function of voltage for a 1.55 mm-long modulator for different values of the input wavelength. c) Experimentally estimated optical losses of the 1.55 mm long modulator, due to the metal layer on the top of the waveguide, as a function of wavelength. The solid red line is an eye guiding.

cadmium telluride (MCT) photodetector (DSS-MCT-020, Horiba), cooled with liquid nitrogen to suppress thermal noise. The resulting electrical signal is then transferred to a lock-in amplifier for synchronous detection. Figure 5(b) shows the relative optical transmission, i.e., the ratio between the optical transmission at a given voltage and the transmission at zero volts, as a function of the reverse bias voltage for wavelengths ranging from 5.5 to 9 µm. As the reverse bias voltage increases, the transmission also increases, reaching an extinction ratio (ER) of approximately 1.9 dB at −12 V for a wavelength of 9 µm in a 1.55-mm-long modulator. Additionally, transmission increases with the wavelength, which is consistent with the expected behavior based on the FCPD effect. The maximum ER occurs at 9 µm because free-carrier absorption becomes stronger with increasing wavelength in the mid-infrared range, as predicted by the Drude model, where absorption scales approximately with λ^2.

The insertion loss of the modulator was estimated experimentally by comparing the optical transmission of two devices that differ only by the presence or absence of the top metallic layer (along the 1.55 mm long modulator). This approach is valid because the top metal layer is the main source of optical loss in the modulator, as will be shown by the measured values presented hereafter. Indeed, as a comparison, typical losses of passive graded SiGe waveguides without any metal layer range from 0.5 to 1.2 dB/cm between 5.5 to 8 µm wavelength, and remain below 2.5 dB/cm up to 9 µm wavelength [15]. The modulator insertion loss is obtained by subtracting the attenuation of the reference waveguide (without the metal contact) from that of the waveguide with the metal on top. The results are shown in Fig. 5(c). Modulator insertion losses range from 2.5 to 7.2 dB for wavelengths varying from 5.5 to 7.8 µm. The increase with the wavelength is

Optics EXPRESS

explained by a larger mode area, which results in a larger overlap between the optical mode and the top metal layer.

Finally, the high-speed performance of the modulator was characterized using two different characterization techniques. The first experiment relies on the experimental setup shown in Fig. 6. Light from a distributed feedback quantum cascade laser (DFB-QCL) operating at 8.5 µm wavelength is coupled to the photonic circuit. A combination of DC and RF electrical signals is applied to the modulator through a bias tee. The DC bias was supplied by a Keithley 2400 source meter, while the RF signal, at frequency f_{RF}, is generated using an AnaPico APULN RF generator. To ensure proper termination, a second RF probe is placed at the output end of the modulator traveling wave electrode and connected to a 50 Ω load through another bias tee. The modulated optical output is then focused on a packaged QWIP [29], which provides both DC and RF access. The QWIP converts the optical signal into an electrical signal, which is analyzed using an electrical spectrum analyzer (ESA) (MS2830, Anritsu).

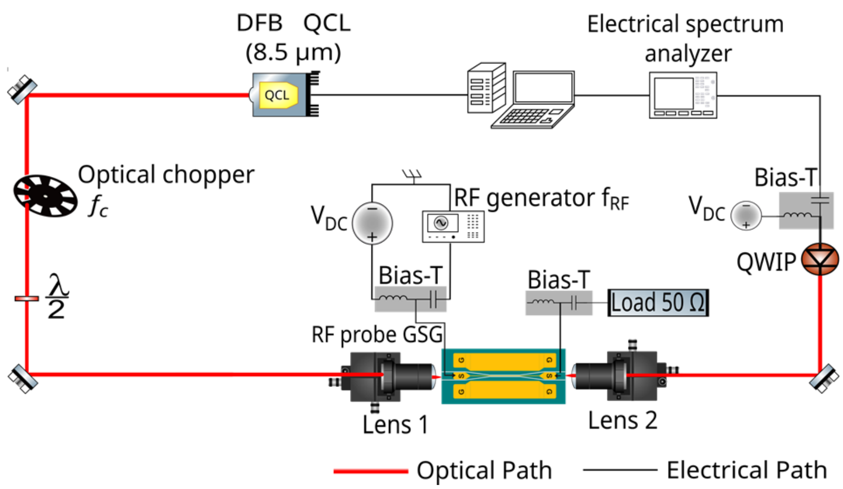

Fig. 6. Experimental setup for dynamic characterization.

While direct measurements of the modulated optical signal at f_{RF} generally suffer from RF antenna effects and radiation coming from the cables, the measurement is instead performed on a lateral sideband. To do so, an optical chopper is placed before the input lens to modulate the incident laser beam at f_c (f_c = 1164 Hz in our experiment). This modulation creates a beatnote at $f_{RF} - f_c$. Measuring the signal at this beatnote frequency improves the measurement sensitivity, as there is less parasitic radiation at $f_{RF} - f_c$ than at f_{RF}. The signal measured on the ESA as a function of f_{RF}, normalized with the response measured at 100 MHz, is reported in Fig. 7(a). For comparison, the measurement floor level, obtained when turning off the input laser, can be seen in blue in Fig. 7(a). Interestingly, the modulated signal is clearly seen, more than 10 dB above the floor level, up to 7 GHz. Beyond this value, the increase in the floor level, which is explained by both the phase noise of the RF generator and by the ESA properties, prevents the measurement of the modulated signal.

To deduce the modulator bandwidth, it should be reminded that the measurement gives the total system response, including the QWIP response as a function of the frequency, which can be seen on Fig. 7(b), but also the RF path response (signal generator and connecting cables) that can be seen on Fig. 7(c). To isolate the dynamic behavior of the electro-optical modulator, the signal measured at the ESA is then normalized by the frequency responses of the QWIP and the RF path, and later divided by a factor of two to take into account the quadratic relation between the optical power at the modulator output and the measured electrical power at the output of

Optics EXPRESS

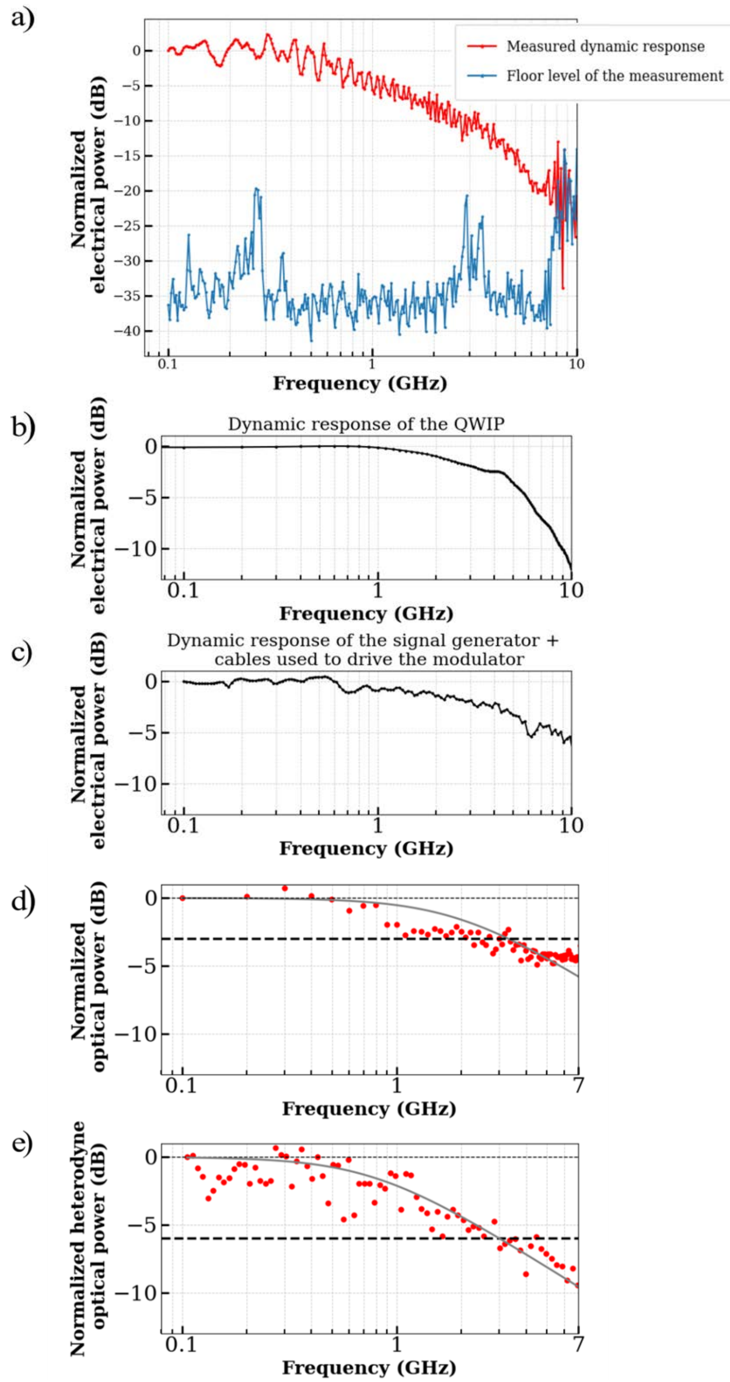

Fig. 7. a) Dynamic characterization of the electro-optical modulator in the depletion regime. b) Dynamic response of the QWIP. c) Dynamic response of the signal generator and the cables used to drive the modulator. d) Normalized optical power output after normalization by the QWIP and signal generator + cable responses, isolating the dynamic behavior of the modulator. e) Normalized optical power output obtained via heterodyne detection.

Optics EXPRESS

the photodetector. The evolution of the modulated optical power at the modulator output as a function of the frequency is then obtained, and shown in Fig. 7(d). Based on this analysis, a 3 dB optical bandwidth of more than 3 GHz is obtained. Interestingly, similar results are observed across devices with lengths ranging from 1.55 mm to 2.3 mm.

Interestingly, a second method has been proposed to analyze the modulator frequency response, based on a heterodyne measurement. To do so, a photonic circuit has been characterized, in which the incident beam is split on-chip using a 1×2 MMI, and each of the resulting beams is modulated by a different modulator. Each modulator consists, similarly to the previously described one shown in Fig. 3, of a 1.5 mm-long device. The modulators outputs are then recombined using a 2×1 MMI. The incident light comes from a CW quantum cascade laser (MIRcat-QT, Daylight Solutions), and both modulators are subjected to a reverse bias of 4 V. Two different RF synthesizers (Anapico APULN and Anritsu MG369xC), sharing the same clock, are outputting 20 dBm sinusoidal signals at frequencies f and $f + \Delta f$, respectively, where Δf is set to 100 MHz. The resulting output is sent to a commercially available MCT detector (Vigo UHSM-I-10.6), connected to the electrical spectrum analyzer, and the power of the beatnote at frequency Δf is recorded as a function of the modulating frequency f. The resulting beatnote is normalized by the dynamic response of electrical circuits including the sources, and the result is shown in Fig. 7(e), where the data points are shown in red and a trend curve following a first order Butterworth filter response is shown in grey, in order to help the reader assessing the trend followed by the data points. It is of great importance to note that since this is the result of the product of two modulation beatnotes, the actual optical bandwidth of the modulator could be estimated at the −6 dB cut-off frequency of this measurement, resulting from the −3 dB cut-off frequency of both modulators. From this measurement, a modulator optical bandwidth of 3 GHz is extracted, exhibiting a good consistency with the direct measurement shown in Fig. 7(d).

5. Discussion

While the demonstration of high speed operation up to 7 GHz, together with a bandwidth of 3 GHz is already a significant improvement in comparison with previous results, it is interesting to analyze the theoretical limitation of the device. Numerical simulations are then reported to evaluate the theoretical electro-optical (EO) response of the modulator. For this purpose, Advanced Design System (ADS) software has been used to model the equivalent transmission line of the modulator. To properly model the propagation of the electrical and optical signals along the modulator, the device was divided into 60 elementary cells, as shown in Fig. 8(a). The signal line width (W) is 4 µm, and the signal-to-ground gap (G) is 30 µm, as in the fabricated device. In each section, the equivalent circuit of the Schottky diode (series resistance, junction resistance and junction capacitance) is integrated into the transmission line model using a scaling factor to consider the length of the elementary cells. The diode series resistance R_S has been experimentally determined to be 15 Ω through current-voltage (I-V) characterization in the injection regime. The junction capacitance C_d has also been experimentally determined to be 4.6×10^{-13} F from capacitance-voltage (C-V) measurements. Finally, the junction resistance, in parallel of C_d, is obtained by fitting the current-voltage characteristic of the diode. A value of 7.3×10^{6} Ω was obtained, but it can be noted that R_j does not play a strong role in the results presented below. Interestingly, it can be noted that the $R_S C_d$ product is approximately 7 ps, which implies high-speed capability of the diode itself. This RC time constant corresponds to a RC-limited 3 dB cutoff frequency of approximately 23 GHz.

Numerical simulations of the transmission line are then presented in Fig. 8(b) to 8(d). It can be seen from Fig. 8(b) that the CPWG achieves impedance matching close to 50 Ω, ensuring compatibility with standard RF characterization equipment. Figure 8(c) shows the S_{21} parameter as a function of RF frequency, demonstrating low-loss RF transmission. Finally, Fig. 8(d) represents the dynamic response, which corresponds to the modulated optical power at the

Optics EXPRESS

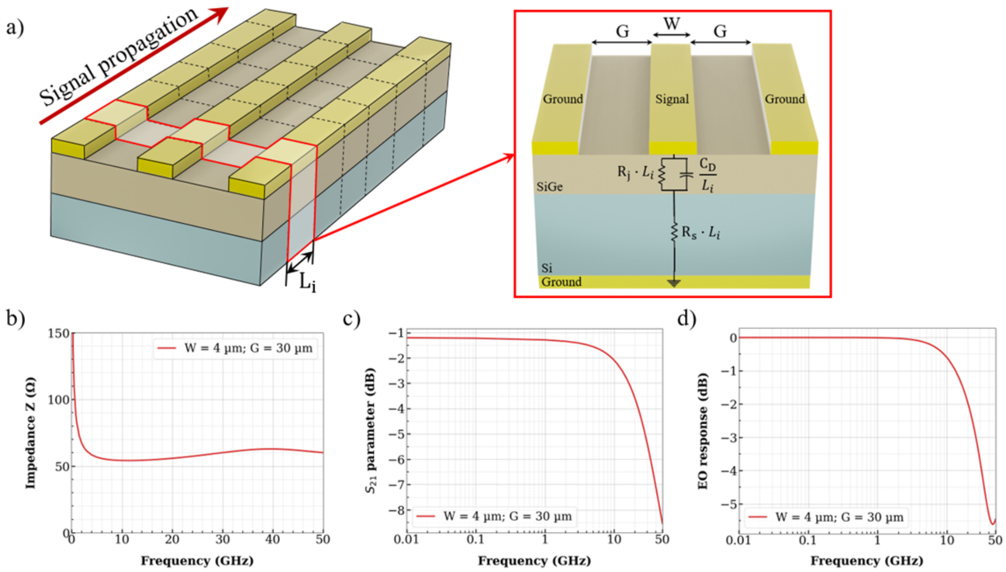

Fig. 8. a) Schematic representation of the device segmented into L_i sections used to calculate the RF properties of the modulator and to monitor the voltage evolution along the propagation. Inset: Cross-sectional view of the CPWG electrodes and the equivalent circuit model of the Schottky diode-based SiGe optical modulator. b-c) Impedance and S_{21} parameter of the device as a function of the RF frequency for the 1.55 mm long modulator. d) Electro-optical (EO) response as a function of the RF frequency, normalized with the value at 10 MHz.

device output as a function of the applied RF frequency. This response is calculated considering the actual dynamic voltage applied to the different sections of the Schottky diode along the device. Interestingly, a −3 dB bandwidth of 26 GHz is obtained from the numerical simulation, which aligns well with the RC-limited bandwidth, and indicates that in this modeling, the charging/discharging time of the Schottky diode is the main limiting factor of the modulator speed.

However, a discrepancy is observed with experiments, where the −3 dB bandwidth is limited to 3 GHz. While the origin of this difference is not fully understood for the moment, the main hypothesis relies on a limitation due to the taper sections used to enlarge the waveguide to apply the external RF electrical probes. Future work should focus in an optimization of these sections to reach bandwidth beyond 20 GHz.

6. Conclusion

In conclusion, this study represents a significant advance in the development of high-performance integrated modulators operating in the long-wavelength range of the mid-IR spectrum. We have experimentally demonstrated efficient modulation with an extinction ratio of up to 1.9 dB at a wavelength of 9 µm, and high-speed operation up to 7 GHz using two different characterization methods. While an optical bandwidth of 3 GHz has been deduced, numerical simulations indicate that it is expected to be greater than 20 GHz. Optimization of the device taper sections will then be pursued in the future. Furthermore, it should be noted that although the high speed measurement was performed at a wavelength of 8.5 µm, the modulation speed of the device is expected to be independent of the operating wavelength. These results pave the way for future progress in areas such as on-chip photonic signal processing, environmental sensing and free-space optical communication within the atmospheric transparency windows (3-5 µm and 8-14 µm).

Funding. HORIZON EUROPE European Innovation Council (101128598 - UNISON); European Research Council (101097569 - Electrophot); French RENATECH network.

Acknowledgment. 'Co-funded by the European Union (ERC-Electrophot (101097569), Horizon Europe-UNISON (101128598)). Views and opinions expressed are however those of the authors only and do not necessarily reflect those of the European Union or the European Research Council. Neither the European Union nor the granting authority can be held responsible for them. This work was partly supported by the French RENATECH network

Disclosures. The authors declare no conflicts of interest.

Data availability. The data that support the findings of this study are openly available at Zenodo repository [30].

References

1. E. Mendes and N. Duarte, "Mid-infrared spectroscopy as a valuable tool to tackle food analysis: a literature review on coffee, dairies, honey, olive oil and wine," Foods **10**(2), 477 (2021).
2. O. A. Jowder, E. K. Kemsley, and R. H. Wilson, "Mid-infrared spectroscopy and authenticity problems in selected meats: a feasibility study," Food Chemisty **59**(2), 195–201 (1997).
3. M. L. Corvec, F. Charpentier, A. Kachenoura, *et al.*, "Fast and non-invasive medical diagnostic using mid-infrared sensor: The AMNIFIR project," IRBM **37**(2), 116–123 (2016).
4. N. Cezard, A. Dobroc, G. Canat, *et al.*, "Supercontinuum laser absorption spectroscopy in the mid-infrared range for identification and concentration estimation of a multi-component atmospheric gas mixture," Proc. SPIE **8182**, 81820V (2011).
5. L. B. Mostaço-Guidolin, L. S. Murakami, A. Nomizo, *et al.*, "Fourier transform infrared spectroscopy of skin cancer cells and tissues," Appl. Spectrosc. Rev. **44**(5), 438–455 (2009).
6. T. Hu, B. Dong, X. Luo, *et al.*, "Silicon photonic platforms for mid-infrared applications," Photonics Res. **5**(5), 417–430 (2017).
7. H. Lin, Z. Luo, T. Gu, *et al.*, "Mid-infrared integrated photonics on silicon: A perspective," Nanophotonics **7**(2), 393–420 (2017).
8. J. S. Penadés, C. A. Ramos, A. Z. Khokhar, *et al.*, "Suspended SOI waveguide with sub-wavelength grating cladding for mid-infrared," Opt. Lett. **39**(19), 5661–5664 (2014).
9. M. Nedeljkovic, A. Z. Khokhar, Y. Hu, *et al.*, "Silicon photonic devices and platforms for the mid-infrared," Opt. Mater. Express **3**(9), 1205–1214 (2013).
10. S. Jung, D. Palaferri, K. Zhang, *et al.*, "Homogeneous photonic integration of mid-infrared quantum cascade lasers with low-loss passive waveguides on an InP platform," Optica **6**(8), 1023–1030 (2019).
11. A. G. Arroyo, E. Baudet, L. Bodiou, *et al.*, "Optical characterization at 7.7 µm of an integrated platform based on chalcogenide waveguides for sensing applications in the mid-infrared," Opt. Express **24**(20), 23109–23117 (2016).
12. R. Soref, "Mid-infrared photonics in silicon and germanium," Nat. Photonics **4**(8), 495–497 (2010).
13. Y. Chang, V. Paeder, L. Hvozdara, *et al.*, "Low-loss germanium strip waveguides on silicon for the mid-infrared," Opt. Lett. **37**(14), 2883–2885 (2012).
14. M. Nedeljkovic, J. S. Penades, V. Mittal, *et al.*, "Germanium-on-silicon waveguides operating at mid-infrared wavelengths up to 8.5 µm," Opt. Express **25**(22), 27431–27441 (2017).
15. M. M. Ballester, V. Vakarin, Q. Liu, *et al.*, "Ge-rich graded SiGe waveguides and interferometers from 5 to 11 µm wavelength range," Opt. Express **28**(9), 12771–12779 (2020).
16. A. S. Postigo, A. O. Moñux, J. S. Penadés, *et al.*, "Suspended germanium waveguides with subwavelength-grating metamaterial cladding for the mid-infrared band," Opt. Express **29**(11), 16867–16878 (2021).
17. N. Koompai, T. H. N. Nguyen, V. Turpaud, *et al.*, "Long-wave infrared integrated resonators in the 7.5-9 µm wavelength range," Appl. Phys. Lett. **123**(3), 031109 (2023).
18. M. M. Ballester, Q. Liu, V. Vakarin, *et al.*, "On-chip Fourier-transform spectrometer based on spatial heterodyning tuned by thermos-optic effect," Sci. Rep. **9**(1), 14633 (2019).
19. M. L. Meade, "Advances in lock-in amplifiers," J. Phys. E: Sci. Instrum. **15**(4), 395–403 (1982).
20. I. J. Bush and R. L. Phillips, "Synchronous phase detection for optical fiber interferometric sensors," Appl. Opt. **22**(15), 2329–2336 (1983).
21. H. Dely, T. Bonazzi, O. Spitz, *et al.*, "10 Gbit s-1 free space data transmission at 9 µm wavelength with unipolar quantum optoelectronics," Laser Photonics Rev. **16**(2), 2100414 (2022).
22. Y. Su, J. Meng, T. Wei, *et al.*, "150 Gbps multi-wavelength FSO transmission with 25-GHz ITU-T grid in the mid-infrared region," Opt. Express **31**(9), 15156–15169 (2023).
23. M. Malerba, S. Pirotta, G. Aubin, *et al.*, "Ultrafast (≈10 GHz) mid-IR modulator based on ultra-fast electrical switching of the light-matter coupling," Appl. Phys. Lett. **125**(4), 041101 (2024).
24. G. V. Georgiev, W. Cao, W. Zhang, *et al.*, "Near-IR & Mid-IR Silicon Photonics Modulators," Sensors **22**(24), 9620 (2022).
25. D. P. Galacho, D. M. Morini, R. Stoffer, *et al.*, "Simplified modeling and optimization of silicon modulators based on free-carrier plasma dispersion effect," Opt. Express **24**(23), 26332–26337 (2016).

Optics EXPRESS

26. T. H. N. Nguyen, N. Koompai, V. Turpaud, *et al.*, "1 GHz electro-optical silicon-germanium modulator in the 5-9 µm wavelength range," Opt. Express **30**(26), 47093–47102 (2022).
27. C. Rosenblad, H. R. Deller, A. Dommann, *et al.*, "Silicon epitaxy by low-energy plasma enhanced chemical vapour deposition," J. Vac. Sci. Technol., A **16**(5), 2785–2790 (1998).
28. M. Kummer, C. Rosenblad, A. Dommann, *et al.*, "Low energy plasma enhanced chemical vapor deposition," Mater. Sci. Eng. B **89**(1-3), 288–295 (2002).
29. Q. Lin, M. Hakl, S. Lepillet, *et al.*, "Real-time, chirped-pulse heterodyne detection at room temperature with 100 GHz 3-dB-bandwidth mid-infrared quantum-well photodetectors," Optica **10**(12), 1700–1708 (2023).
30. J. Huertas-Pedroche, V. Turpaud, L. Lucia, *et al.*, "Dataset for High-speed integrated silicon germanium optical modulator with 3 GHz bandwidth in the 5-9 µm wavelength range," Zenodo (2025), https://zenodo.org/records/17119589